

Extending the Inductor Operating Frequency for Optimally-coupled Wireless Power Transfer Systems

Fabian L. Cabrera, Renato S. Feitoza and F. Rangel de Sousa

Electrical Engineering Department
Federal University of Santa Catarina
Florianópolis-SC, 88040-900, Brazil.

E-mail: fabian.l.c@ieee.org, renato.feitoza@grad.ufsc.br, rangel@ieee.org

Abstract—This paper presents a technique for extending the operating frequency of an inductive link used for wireless power transfer. The extension is achieved by segmenting the primary inductor. A circuit model is proposed for a single-coil squared inductor, which provides the basis for the model of the segmented inductor. These models help to understand the operation of the segmented inductor and serve as a guide to its design. A prototype of the link was fabricated, in which the primary inductor has an average diameter of 22 mm and four segments. The secondary inductor has an average diameter of 4 mm and the two inductors are expected to be optimally coupled at the distance of 15 mm. The operating frequency was experimentally validated to be 980 MHz which is higher than the 415 MHz measured for a conventional inductive link of same dimensions, while the link efficiency is maintained at the same value of 30%.

I. INTRODUCTION

Inductive links have been widely used for wireless power transfer (WPT) to implanted medical devices (IMDs) [1] and to radio-frequency identification (RFID) tags [2], among others. A primary inductor transfers energy via magnetic coupling to a secondary inductor, which is located at the implant (or at the tag in case of RFID applications). According to this definition, both sides of the inductive link have different restrictions, for instance the secondary inductor must be miniaturized to reduce the size of the implant or the tag. On the other hand, the area restriction of the primary inductor is more relaxed. This leads to asymmetrical links, which is relevant for the main figure of merit: the power transfer efficiency (η).

The value of η depends on the electromagnetic coupling level of the link (A) and on the load impedance matching condition (p) as can be verified by the reciprocal of the efficiency calculated by [3]:

$$\frac{1}{\eta} = \frac{1}{A} \left(p + 2 + \frac{1}{p} \right) + p + 1. \quad (1)$$

In (1), $A = k^2 Q_1 Q_2$, where k is the magnetic coupling factor and Q_1 and Q_2 are the quality factors of the primary and secondary inductors, respectively. Those three components must be maximized to maximize A and hence the efficiency. The k value depends mainly on the geometry of the inductors and the distance between them (d). Hence, depending on the value of d there is a proportion between the primary and secondary inductor sizes that optimizes k [3], reinforcing the idea that the link has to be asymmetrical. Moreover, the quality

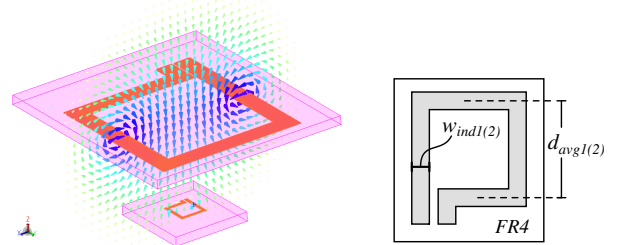


Fig. 1. (a) Magnetic field at the inductive link. (b) Inductors Geometry.

factor (Q) of an inductor depends on its dimensions and on the frequency (f). For a fixed-size inductor, Q increases with f from DC until a point so-called optimum, where Q starts to decrease due to the radiation losses. Above the optimal point, the current through the entire coil is no longer uniform. The frequency where the optimal point occurs depends on the coil perimeter, limiting the operating frequency of big inductors to lower frequencies. Given that the inductive link is asymmetrical, the operating frequency is restricted by the largest inductor [3]. As we demonstrate in this work, that limitation may be overcome by using a segmented inductor.

Segmented inductors also can be referred in literature as segmented loop antennas [4–5]. In [4], the SAR (*Specific Absorption Rate*) level in biological tissues is reduced by using a segmented inductor to powering an IMD. That reduction is achieved because instead of having one capacitor, the segmented inductor has several capacitors in series, thus better distributing the electrical field along the coil. In [5] a loop antenna is segmented to keep uniformity of the current magnitude and phase along the loop, thus improving the magnetic field distribution on the antenna near-field region.

In this paper we demonstrate the extension of the operating frequency of a WPT link by using a segmented inductor. A model for the non-segmented planar inductor is proposed in Section II. The theory and design of the segmented planar inductor is shown in Section III, leading to the experimental results of section IV. The conclusions are drawn in Section V.

II. PLANAR INDUCTOR MODELING

In this section we develop a model for the k and Q factors. The inductors are positioned as shown in Fig. 1(a). Each

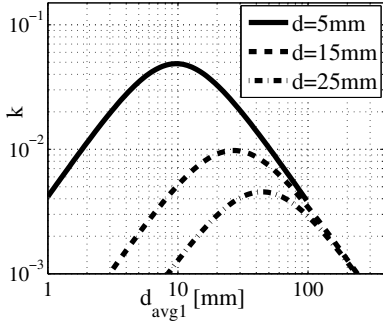


Fig. 2. Magnetic coupling factor when $d_{avg2} = 4$ mm.

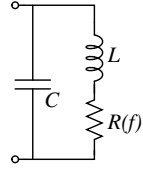


Fig. 3. Broadband inductor model.

single-turn inductor $L_{1(2)}$ has width $w_{ind1(2)}$ and average diameter $d_{avg1(2)}$, as sketched in Fig 1(b).

A. Magnetic coupling factor

The value of k is equivalent to $M/\sqrt{L_1 L_2}$, where M is the mutual inductance between L_1 and L_2 . The mutual inductance is given by (2) and (3):

$$M = \mu \sqrt{\frac{d_{avg1} d_{avg2}}{\pi}} \left[\left(\frac{2}{\gamma} - \gamma \right) K(\gamma) - \frac{2}{\gamma} E(\gamma) \right] \quad (2)$$

$$\gamma = \sqrt{\frac{4 d_{avg1} d_{avg2}}{(d_{avg1} + d_{avg2})^2 + \pi d^2}}, \quad (3)$$

where $K(\gamma)$ and $E(\gamma)$ are complete elliptic integrals of the first and second kind, respectively; γ is their argument and μ is the magnetic permeability. These equations are based on the analytical solution for the mutual inductance between two single-turn circular coils [6]. The equivalence from circular to rectangular shapes was done by keeping the same enclosed area for each coil. The curves of k as a function of d_{avg1} are plotted in Fig. 2 for three distances between inductors. The size of the secondary inductor is the same as in [3], which is $d_{avg2} = 4$ mm and $w_{ind2} = 0.5$ mm.

B. Quality factor

A broadband model for a planar inductor is shown in Fig. 3, where L is the inductance at DC. The resistance $R(f)$ accounts for both ohmic and radiation losses, and the capacitor C models the self-resonant frequency (SRF), which is the frequency after that the equivalent reactance is no longer inductive. At the SRF the average loop perimeter is equal to half of the effective wavelength (λ_{eff}) of signal traveling along the inductor. This condition can be written as

$\frac{\lambda_{eff}}{2} \approx 4d_{avg1}$ for the case of inductor drawn in Fig. 1(b). The inductor losses can be described by (4):

$$R = R_{DC} F_{skin} F_r + R_{rad}. \quad (4)$$

In (4) we can identify four terms: the DC resistance R_{DC} ; two factors F_{skin} and F_r modeling respectively the skin and radial redistribution of current in the conductor cross section; and the radiation resistance R_{rad} . The value of R_{DC} is given by (5):

$$R_{DC} = \frac{\rho(4d_{avg})}{w_{ind} t_c}, \quad (5)$$

where ρ and t_c are the conductor resistivity and thickness, respectively. The skin effect factor (F_{skin}) is given by (6) and (7) [7]:

$$F_{skin} = \frac{t_c}{2\delta} \frac{\sinh(t_c/\delta) + \sin(t_c/\delta)}{\cosh(t_c/\delta) - \cos(t_c/\delta)} \approx \frac{t_c}{2\delta} \quad (6)$$

$$\delta = \sqrt{\frac{\rho}{\pi f \mu}}, \quad (7)$$

where δ is called the skin depth. The approximation done in (6) is valid when t_c is significantly greater than δ . On the other hand, the current has a distribution profile in the radial direction, this is depending on the distance from the inductor center to the conductor section, this profile is different in high frequencies compared to the DC profile. For this reason we added the factor F_r in (4). As this effect has not been derived analytically, we can use an empirical model:

$$F_r = \alpha w_{ind}^{\beta_1} f^{\beta_2}, \quad (8)$$

where α , β_1 and β_2 are parameters obtained from curve fitting of the electromagnetic simulations on a set of inductors. We chose a set of inductors with d_{avg1} varying between 4 mm and 30 mm, and w_{ind1} varying between 0.3 mm and 4.5 mm. For this set, the adjusted model constants are: $\alpha = 128$, $\beta_1 = 0.3$ and $\beta_2 = -0.1$.

The radiation resistance was calculated in [8] for a circular inductor. The equivalence from circular to squared shapes can be done by keeping the same perimeter, that is, if the circular inductor radius is r_c then $2\pi r_c = 4d_{avg}$, so $r_c = 2d_{avg}/\pi$. Finally, the equivalent resistance is shown in (9):

$$R = 256\sqrt{\pi\rho\mu} d_{avg} w_{ind}^{-0.7} f^{0.4} + \frac{128\pi}{3} \sqrt{\varepsilon^3 \mu^5} f^4 d_{avg}^4 \quad (9)$$

Regarding the inductance, it is given by (10) [9]:

$$L = \frac{2d_{avg}\mu}{\pi} \ln \left(\frac{0.59\pi d_{avg}}{w_{ind}} \right) \quad (10)$$

Using (9) and (10) we can calculate the loss factor (Λ) which is the reciprocal of Q . The Λ value is equal to $R/(2\pi f L)$ resulting in:

$$\Lambda = 64 \sqrt{\frac{\pi\rho}{\mu}} \frac{w_{ind}^{-0.7} f^{-0.6}}{\ln \left(\frac{0.59\pi d_{avg}}{w_{ind}} \right)} + \frac{32\pi}{3} \frac{\sqrt{\varepsilon^3 \mu^3} f^3 d_{avg}^3}{\ln \left(\frac{0.59\pi d_{avg}}{w_{ind}} \right)}. \quad (11)$$

Analyzing this equation, we can see that the first term is dominant at low frequencies and has a decreasing characteristic

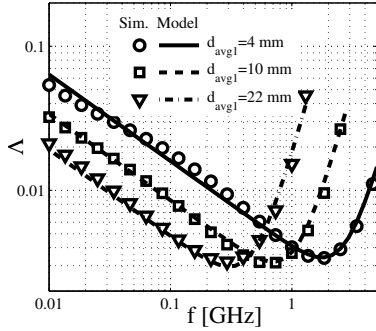


Fig. 4. Loss factor comparison between model and EM simulations.

with frequency ($f^{-0.6}$). The second term is dominant at higher frequencies and has a positive slope (f^3). In Fig. 4 the loss factor modeled with (11) and the electromagnetic simulations done in the software EMPRO® of Keysight® are compared. As observed, the model is in agreement with the simulation results. The minimum loss factor (Λ_{min}) for a inductor is calculated from (11), it occurs at the frequency $f_{\Lambda min}$:

$$f_{\Lambda min} = \left(\frac{0.46 \rho}{\varepsilon^3 \mu^4 d_{avg}^6 w_{ind}^{1.4}} \right)^{1/7.2}. \quad (12)$$

It can be noted that $f_{\Lambda min}$ depends mainly on d_{avg} , μ and ε . Replacing (12) into (11) we can calculate Λ_{min} :

$$\Lambda_{min} = \frac{145.3}{\ln \left(\frac{0.59 \pi d_{avg}}{w_{ind}} \right)} \left(\frac{\rho^5 \varepsilon^3 d_{avg}^6}{\mu^2 w_{ind}^7} \right)^{1/12}, \quad (13)$$

which depends mainly on (d_{avg}/w_{ind}) , ρ , ε and μ . The above means that, excluding the logical choice of the value of d_{avg}/w_{ind} that optimizes (13), the minimum loss factor only depends on the technology parameters. On the other hand, $f_{\Lambda min}$ is strongly dependent on d_{avg} . This limitation on the operating frequency of inductors may be overcome by segmenting the wire.

III. SEGMENTED INDUCTOR: THEORY AND DESIGN

In this section we explore the basic concepts about segmented inductors, its design considerations and its effects on link efficiency. In the numerical examples, we use $d_{avg1} = 22$ mm, $w_{ind1} = 2.8$ mm, $d_{avg2} = 4$ mm and $w_{ind2} = 0.5$ mm to keep a comparative point with results obtained in [3]. A planar inductor can be segmented by adding small gaps equally separated as shown in Fig. 5(a) for the four-segments case. Discrete capacitors C_D are soldered in each gap, connecting the segments and adjusting the series-resonant frequency. That capacitance, together with the gap capacitance (C_G), is represented by $C_S = \frac{C_D + C_G}{N - 1}$ in the segmented inductor model of Fig. 5(b), where N is the number of segments. When $N = 1$ then C_S tends to ∞ , which means that it must be replaced by a short-circuit in the model. The L and C components do not change significantly with respect to the model of Fig. 3. The losses are modeled with the resistor $R_S(f, C_S)$ which depends

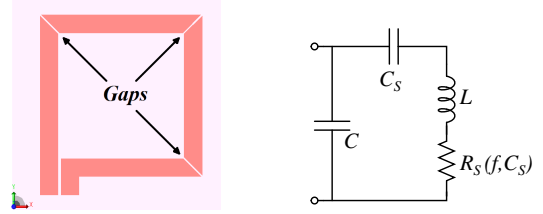


Fig. 5. (a) Four-segments inductor. (b) Segmented inductor model.

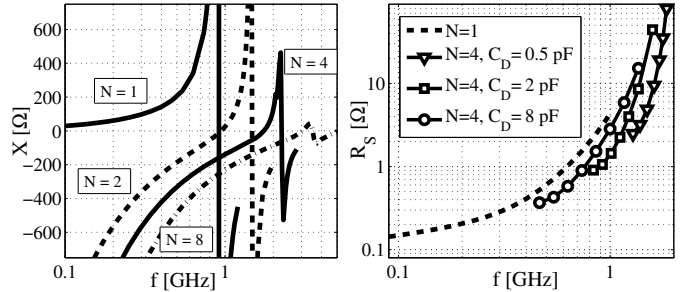


Fig. 6. (a) Equivalent reactance when $C_D=0$. (b) Segmented inductor losses.

on the frequency and on the capacitance C_S . The effect of C_S on R_S appears as a change on the radiation profile of the inductor.

The first consequence of segmenting the inductor can be perceived from the circuit of Fig. 5(b). The circuit presents a series-resonant frequency at $\omega = 1/\sqrt{LC_S}$ and a parallel-resonant frequency at $\omega = 1/\sqrt{LC_e}$, where C_e is the equivalent series capacitance between C and C_S . Since C_e is smaller than C , the SRF is increased. A greater value of N means a smaller value of C_S and hence a higher SRF. This can be verified in Fig. 6(a), where the equivalent reactance of segmented inductors is compared with the one-segment case. The working frequency must be chosen between the series and parallel resonance, in order to guarantee that the coil is indeed operating as an inductor.

The second consequence can be seen in Fig. 6(b), where we compare the R_S curves of a four-segment inductor with the one-segment inductor for several values of C_D . The R_S curve is shifted to the right when using four segments, but this deviation depends on the C_D value. As C_D tends to infinity the R_S curve tends to the R curve of the one-segment inductor. This is due to the fact that large capacitance couples the signal so strongly that it behaves almost like a short-circuit, i.e., virtually is like there are no gaps. The shift on the resistance curves is explained by changes in the radiation resistance: when the loop perimeter $4d_{avg1}$ is much shorter than $2\pi/\lambda_{eff}$, the current distribution is constant and, as a consequence, the near-fields are very concentrated, while the far-fields tend to be canceled. As the perimeter increases, the current distribution starts presenting nulls and phase-inversions, the near-fields are not even anymore and the far-fields are no longer canceled, hence there is higher radiation

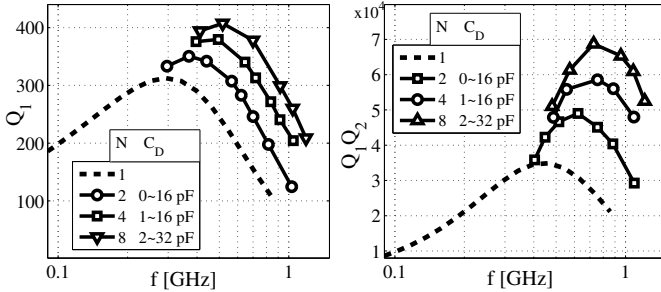


Fig. 7. (a) Segmented inductor quality factor. (b) Multiplied by the secondary inductor quality factor.

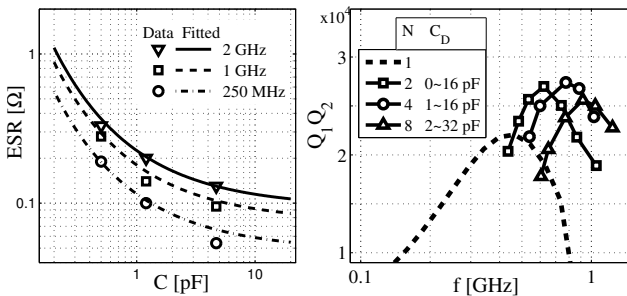


Fig. 8. (a) Equivalent series resistance for discrete capacitors. (b) Quality factors product accounting the capacitors ESR.

and consequently higher radiation resistances. When the loop is segmented, the capacitor compensates for the phase changes caused by the inductor, and if correctly designed, the current along the loop can be in-phase even in a loop that is not electrically small. It follows that a lower radiation resistance is expected for the segmented case.

Considering the R_S values obtained from electromagnetic simulations we can calculate the quality factor of primary inductor ($Q_1 = 2\pi f L / R_S$) as shown in Fig. 7(a). Noting that each mark corresponds to the maximum quality factor for each value of C_D , legend shows the range of C_D values for each curve. As the radiation resistance is decreased by augmenting N , the quality factor is improved as well as the frequency where its maximum occurs is increased. Moreover, if we multiply the primary (segmented) and secondary inductor quality factors as plotted in Fig. 8(b), the benefits of using the segmented inductor become more evident. However, the results showed in Fig. 7(b) consider ideal capacitors, so real capacitors can change perspectives.

For the link implementation we count on high-quality factor capacitors in SMD 0402 package. The equivalent series resistance (ESR) of capacitors is informed by the manufacturer for some capacitors, marked as “Data” in Fig. 8(a). This information must be extrapolated to the entire range of capacitors that can be used. That extrapolation is plotted as curves in the same figure. Adding the effects of the capacitor ESR, the curves of Fig. 7(b) turn to the curves of Fig. 8(b). In all curves a decrease in $Q_1 Q_2$ value is noticeable, especially

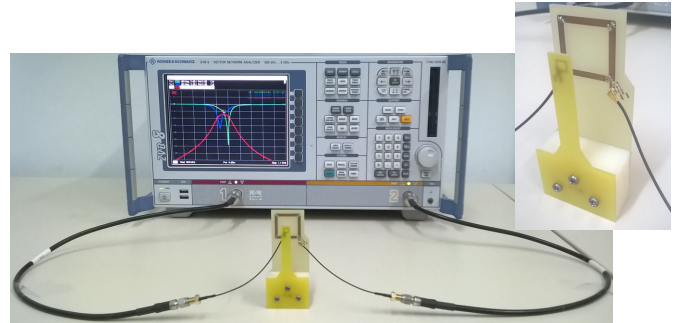


Fig. 9. Link test setup and detail of the four-segments inductor.

for larger values of N because it increases the number of capacitors in series, thus increasing the equivalent resistance. Taking into account the results of Fig. 8(b), the best link efficiency for the inductor dimensions selected can be obtained when the primary inductor has four segments and the operating frequency is approximately 800 MHz with a C_D value of 3 pF.

IV. EXPERIMENTAL RESULTS

Although the analysis done in the previous section pointed out 800 MHz as being the optimum frequency, the prototype for experimental verification was designed to operate at 1 GHz. The reason for this choice was that the primary inductor also serves to transfer energy to the integrated wireless power receiver designed in [10], which includes an integrated LC resonator characterized in [11]. To operate at 1 GHz the capacitors C_D must be chosen to be 1.5 pF. The fabricated prototype and the measurement setup are shown in Fig. 9. A R&S® ZVB8 vector network analyzer (VNA) is used to measure the S-parameters. The two inductors are matched to the 50 Ω measurement system by using capacitive L-networks. The S-parameters measured are shown in Fig. 10. In the ideal case, the two inductors must be matched at the same frequency, but in practice it is very difficult to achieve this situation with fixed value capacitors. For this reason, the link efficiency is calculated as the maximum achievable gain (MAG) from the S-parameters.

In Table I are compared the measured results with full-wave electromagnetic simulations done in EMPRO®. According to simulations, the highest efficiency that can be achieved for the inductor dimensions specified is 38% at the frequency of 735 MHz and using a four-segments inductor. When operating the four-segments inductor around 1 GHz, the link efficiency slightly drops to 37%. However, the link efficiency measured only achieves the value of 30%. The difference between measurements and simulation can be attributed to parasitic components difficult to simulate, as the resistance and the capacitance added by the weldings. Despite this, it was demonstrated the extension of the link operating frequency by using the segmentation technique.

V. CONCLUSION

The operating frequency of an optimally-coupled inductive link was extended from 415 MHz to 980 MHz, as verified

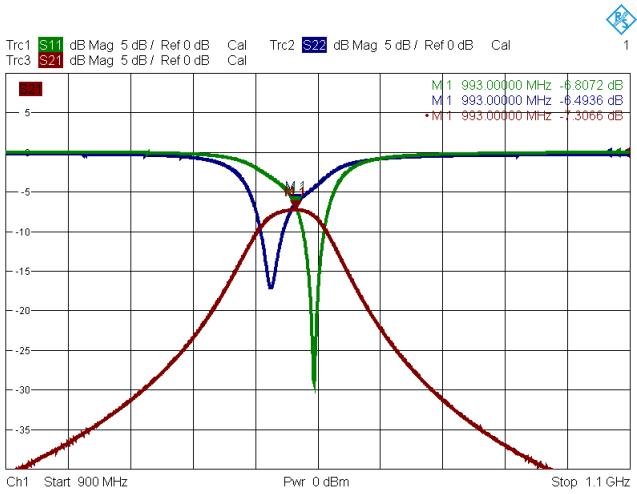


Fig. 10. S-parameters measured of the inductive link.

TABLE I
PERFORMANCE SUMMARY OF THE INDUCTIVE LINK WITH SEGMENTED PRIMARY INDUCTOR.

N	C_D [pF]	η_{max} [%]	$f_{\eta_{max}}$ [MHz]	
1	—	30	415	Meas. [3]
4	3	38	735	Sim.
4	1.5	37	990	Sim.
4	1.5	30	980	Meas.

experimentally. This extension is achieved by dividing the primary inductor into four segments. The link efficiency was measured to be 30 % which is the same efficiency measured in the lower frequency system. Despite not having achieved an improvement in the link efficiency, the technique offers potential improvements that could be exploited with lower ESR capacitors. Moreover, the extension of the primary inductor operating frequency offers flexibility to the inductive link design. For example, the integrated wireless power received was designed at a fixed frequency [10], and it could be magnetically coupled with different primary inductors, including the four-segments inductor designed in this work.

ACKNOWLEDGMENT

This work was partially supported by CNPq, INCT NAMITEC and CAPES.

REFERENCES

- [1] A. Yakovlev, Sanghoek Kim, and A. Poon, "Implantable biomedical devices: Wireless powering and communication," *Communications Magazine, IEEE*, vol. 50, no. 4, pp. 152–159, 2012.
- [2] P. Scholz, C. Reinhold, W. John, and U. Hilleringmann, "Analysis of Energy Transmission for Inductive Coupled RFID Tags," in *RFID, 2007. IEEE International Conference on*, Mar. 2007, pp. 183–190.
- [3] Fabian L. Cabrera and F. Rangel de Sousa, "Optimal Design of Energy Efficient Inductive Links for Powering Implanted Devices," in *Biomedical Wireless Technologies, Networks, and Sensing Systems (BioWireless), 2014 IEEE Topical Conference on*, Jan. 2014, pp. 1–3.
- [4] M. Mark, T. Björninen, L. Ukkonen, L. Sydanheimo, and J.M. Rabaey, "SAR reduction and link optimization for mm-size remotely powered wireless implants using segmented loop antennas," in *Biomedical Wireless Technologies, Networks, and Sensing Systems (BioWireless), 2011 IEEE Topical Conference on*, Jan. 2011, pp. 7–10.

- [5] Xianming Qing, Chean Khan Goh, and Zhi Ning Chen, "A Broadband UHF Near-Field RFID Antenna," *Antennas and Propagation, IEEE Transactions on*, vol. 58, no. 12, pp. 3829–3838, Dec. 2010.
- [6] Clayton R. Paul, *Inductance: Loop and Partial*. Wiley, 2010.
- [7] Hamdi Altayib Abdelbagi, "Skin and proximity effects in two parallel plates," M.Sc. Thesis, Wright State University, 2007. [Online]. Available: https://etd.ohiolink.edu/rws_etd/document/get/wright1190054809/attachment
- [8] Simon Ramo, John R. Whinnery, and Theodore V. Van Duzer, *Fields and Waves in Communication Electronics*. Wiley, Jan. 1994.
- [9] R. Dengler, "Self inductance of a wire loop as a curve integral," *ArXiv e-prints*, Apr. 2012. [Online]. Available: <http://arxiv.org/pdf/1204.1486v2>
- [10] Fabian L. Cabrera and F. Rangel de Sousa, "A CMOS Fully-Integrated Wireless Power Receiver for Autonomous Implanted Devices," in *Circuits and Systems (ISCAS), 2014 IEEE International Symposium on*, June 2014, pp. 1–4.
- [11] Fabian L. Cabrera and F. Rangel de Sousa, "Contactless Characterization of a CMOS Integrated LC Resonator for Wireless Power Transferring," *Microwave and Wireless Components Letters, IEEE*, vol. 25, no. 7, pp. 475–477, July 2015.